ARTICLE IN PRESS

ISA Transactions xxx (xxxx) xxx

Contents lists available at ScienceDirect

ISA Transactions

journal homepage: www.elsevier.com/locate/isatrans

Research article

Artificial intelligence-based nonlinear control of renewable energies and storage system in a DC microgrid

Syeda Shafia Zehra [a], Aqeel Ur Rahman [a], Hammad Armghan [b], Iftikhar Ahmad [a,*], Umme Ammara [a]

[a] School of Electrical Engineering and Computer Science (SEECS), National University of Sciences and Technology (NUST), Islamabad, Pakistan
[b] School of Electrical Engineering, Shandong University, Jinan, China

ARTICLE INFO

Article history:
Received 7 October 2020
Received in revised form 5 April 2021
Accepted 5 April 2021
Available online xxxx

Keywords:
Renewable energy generation
Energy storage system
DC microgrid
Energy management
Fuzzy logic control
Nonlinear supertwisting sliding mode controller

ABSTRACT

To minimize the global warming and the impact of greenhouse effect, renewable energy sources-based microgrids are widely studied. In this paper, the control of PV, wind-based renewable energy system and battery, supercapacitor-based energy storage system in a DC microgrid have been presented. Maximum power points for PV and wind have been obtained using neural network and optimal torque control, respectively. Nonlinear supertwisting sliding mode controller has been presented for the power sources. Global asymptotic stability of the framework has been verified using Lyapunov stability analysis. For load-generation balance, energy management system based on fuzzy logic has been devised and the controllers have been simulated using MATLAB/Simulink® (2019a) along with a comparison of different controllers. For the experimental validation, controller hardware-in-the loop experiment has been carried out which validates the performance of the designed system.

1. Introduction

With the tremendous increase in electricity consumption, depleting oil resources, and the greenhouse effect, the production of electricity from non-renewable energy sources or fossil fuels is shifting to green renewable energy sources (RESs) [1]. In the last two decades, the distributed generation (DG) approach is playing an important part in the changeover from conventional power generation to clean power generation. RESs such as solar and wind energy are found around the globe in abundance which are the main contributors towards improved carbon sustainability [2,3]. They are integrated as DG units with ESSs and loads to form a microgrid (MG). The main advantages of MGs include higher reliability, autonomous control, and ability to meet the load demands in both the islanded and grid-connected modes [4,5]. They are categorized into Direct Current (DC) and Alternating Current (AC) MGs. DC MGs have gained tremendous popularity in remote locations due to higher efficiency, lower cost, and absence of reactive power [6].

In the literature, DG system working with wind power generation as a single RES has been studied [7]. In the absence of sufficient wind power, the system is dependent on the energy storage system (ESS) resulting in an adverse effect on its capacity. It has been observed that the complete dependence of the system on ESS affected its sizing [8]. DG system with PV as the main RES has been studied [9,10] but due to solar energy's intermittent nature, it cannot be implemented without ESS. It is conventional to use a hybrid system with wind and PV as RESs which can mediate the power balance and reduce the size of ESS [11,12] having battery and supercapacitor (SC) to complement each other and are known for their high energy and high power density respectively. The battery provides energy when RESs fail to provide it while SC compensates the variations in power transients at the time of power consumption or production [13,14]. PV system's output power is affected by different environmental parameters such as temperature and the solar irradiance. The output of the wind energy system greatly depends upon the wind speed and torque. To ensure maximum efficiency and power balance in a MG, PV and wind energy systems should be operated at their maximum power point (MPP). Extensive research has been conducted to find efficient maximum power point tracking (MPPT) algorithms which include linear and nonlinear controllers, conventional algorithms and algorithms based on artificial intelligence (AI) and fuzzy logic control. Due to the unpredictable nature of RESs, AI-based algorithms outperform the aforementioned algorithms [15,16].

AC, DC and AC/DC MGs have been implemented worldwide depending upon the load requirements and location. It has been

* Corresponding author.
E-mail addresses: szehra.msee18seecs@seecs.edu.pk (S.S. Zehra), arahman.msee17seecs@seecs.edu.pk (A.U. Rahman), 14mseeharmghan@seecs.edu.pk (H. Armghan), iftikhar.rana@seecs.edu.pk, linkrana@gmail.com (I. Ahmad), uarshad.msee18seecs@seecs.edu.pk (U. Ammara).

https://doi.org/10.1016/j.isatra.2021.04.004
0019-0578/

Please cite this article as: S.S. Zehra, A.U. Rahman, H. Armghan et al., Artificial intelligence-based nonlinear control of renewable energies and storage system in a DC microgrid. ISA Transactions (2021), https://doi.org/10.1016/j.isatra.2021.04.004.

Nomenclature

Variables

V_{in}	Wind rectifier input voltage
I_{pv}	PV panel current
V_b	Voltage of the battery
V_{sc}	Voltage of the supercapacitor
V_{DC}	Voltage of the DC bus

Abbreviations

MG	Microgrid
DG	Distributed Generation
AI	Artificial Intelligence
PV	Photo-Voltaic
ESS	Energy Storage System
RESs	Renewable Energy Sources
MPPT	Maximum Power Point Tracking
EMS	Energy Management System
SC	Supercapacitor
SoC	State of Charge
STSMC	Supertwisting Sliding Mode Controller
C-HIL	Controller Hardware-in-the Loop

RESs - ESS parameters

C_w, C_{pv}, C_{pout}	Input and output capacitances of RESs system
C_{DC}	Filter capacitance of ESS system
L_w, L_{pv}	Inductances of RESs system
L_b, L_{sc}	Inductances of ESS system
R_w, R_{pv}	Series resistances of RESs system
R_b, R_{sc}	Series resistances of ESS system

STSMC parameters

a_1, a_3, a_6, a_7	Design constants of sliding surfaces
$k_{i(i=1,2..,9)}$	Constant controller gains
$\alpha, \beta, \zeta, \gamma$	STSMC gains
$\phi_1, \phi_3, \phi_6, \phi_7$	Constants of reaching law

observed that power transformers are required for the connection of AC MGs with the AC system and an inverter is required to connect it with the DC load [17]. In DC MGs, the power conversion process gets eliminated and the DC based DG units and loads is connected directly with the DC bus. Moreover, they eliminate the need for a transformer contributing to the overall down-sizing of the system with fewer harmonics due to inverters. To wind up, it can be observed that the DC MGs outperform AC MGs in terms of system's cost, efficiency and down-sizing [6,18].

The main objective in a DC MG is to maintain power-sharing between DG units and load which can be obtained with the help of achieving the stability of the DC bus by maintaining it at a constant voltage [19]. For this purpose, substantial research has been conducted using various control techniques. An observer-based droop control has been applied to control the DC bus voltage of a simple MG with two storage units [20]. The trade-off between load sharing accuracy and stability has been addressed but the addition of RESs in the proposed system has not been studied. The DC MG's stability analysis considering constant power loads (CPLs) has been done by solving complex optimization techniques [21]. Due to the negative impedance effect of CPLs, their stability analysis has been done on a defined range and local stability of the MG has been found for a linearized system neglecting the nonlinear nature of RESs. Robust control strategy for control of energy units in a DC MG has been studied by considering a generalized model for the distributed energy resources [22] where stability analysis has been done using a defined set of eigenvalues for a linearized model. A considerable amount of work has been done by applying various linear control techniques on the nonlinear nature of power converters integrated with DG units [23,24] as well as fuzzy-based H_∞ control for nonlinear system [25], fuzzy-based exponential stabilization [26], and sampled-data control of nonlinear systems [27]. Studies have been conducted having a generalized model for DG units neglecting the unpredictable nature of RESs and control strategy which needs to be adopted to cater to the power imbalance [20,22,23].

To mitigate the issues mentioned in case of linear control techniques, extensive research has been conducted using nonlinear control techniques. A robust nonlinear controller has been designed for the control of power sources in a DC MG with a PV panel using the standard MPPT Incremental Conductance Algorithm for the voltage of PV array [28]. Passivity-based nonlinear controller has been studied where it was observed that the DC bus voltage failed to remain at a constant voltage as well as no global stability of the system has been shown [29]. A nonlinear backstepping controller has been studied with the integration of the wind energy system [30] which lacked the behavior of the controller under multiple DG units and a control management strategy for spontaneous power sharing. Adaptive backstepping based nonlinear controller for islanded DC MG has been studied with solar energy as a single DG unit [31]. In this study, MPPT of PV array has not been performed, therefore maximum power cannot be provided by DG unit to load under variations in solar irradiance and temperature. A nonlinear sliding mode control has also been studied [32] in which fluctuations in DC bus voltage have been observed due to the absence of electric-based energy storage system which can provide fast power transients during high load demand. By adjusting the gains of the sliding surface, the sensitivity of the system to the external disturbances can be reduced with SMC. A fuzzy-SMC controller has been studied for the control of MG having multiple RESs along with ESS and electric vehicle but no analysis has been done to evaluate the stability of DC bus voltage under varying environmental conditions [33].

Keeping in mind the aforementioned drawbacks of the previous studies and to study the operation and control of RESs integrated with ESS, a novel energy management system based on fuzzy logic has been presented in this paper which assists the supertwisting sliding mode control (STSMC) algorithm. STSMC displays robustness to all the parametric variations as well as external disturbances because the sliding surface along with its derivative converge to zero in finite time. RESs integrated with the MG are operating at their MPP using AI-based algorithm to obtain maximum efficiency throughout the day in the presence of disturbances caused by environmental variations. An energy management system based on fuzzy logic has been devised which maintains the power balance by providing the desired current references reference according to the state of charges (SoCs) of the battery, SC and the load power demands. The novelty of this work can be summarized into the following aspects:

(1) Global consistency is not exhibited by the linear controllers in their performance which is desired by the ESS as they operate over a wide range;
(2) To maintain the load-generation balance, the RESs and ESS work together by providing reference currents accordingly;
(3) If the power distribution between the HESS and RESs is not managed properly, the system might lead towards instability therefore, an effective energy management algorithm is needed along with the controller;

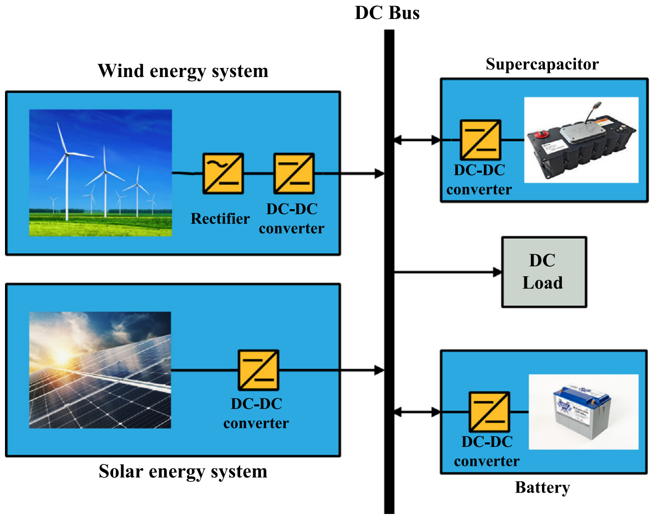

Fig. 1. Formation of a DC MG with RESs and ESS.

(4) The proposed STSMC controller along with an energy management system based on fuzzy logic surpass the linear controllers in terms of the global asymptotic stability which is proved by the Lyapunov stability analysis. Furthermore, the ESS helps the RESs to achieve the goal of this system which is to provide power to the load autonomously;
(5) To validate the real-time implementation of the designed framework, controller hardware-in-the loop (C-HIL) experiment has been carried out.

The basic structure of DC MG has been shown in Fig. 1. The PV array has been connected to the DC bus through a DC-DC buck-boost converter and a DC-DC boost converter has been used to connect DC bus with the wind turbine system. ESSs have been used to reduce the stress on RESs under high load demands and are integrated with the DC-DC buck-boost converters to allow the devices to charge/discharge.

The remaining part of this article has been arranged as follows: Section 2 studies the RESs and ESSs integrated to form a DC MG, Section 3 presents the mathematical model of DC MG, Section 4 studies the design of the proposed controller with an efficient energy management system, Section 5 demonstrates the simulation as well as experimental C-HIL results and Section 6 gives a summary of work done along with some future prospects.

2. Components of DC microgrid

The components considered in this DC MG along with the power converters required for their control and integration with DC bus, have been shown in Fig. 2. The characteristics and the contribution of each source has been explained below.

2.1. Wind energy system

The wind is one of the main contributors towards renewable power generation. The earth's surface generates an air current which is responsible for the wind energy. Wind turbines harvest this kinetic energy and convert it into electrical power. Due to its clean energy generation, the use of a wind energy system has been increasing. The configuration of the wind energy system has been shown in Fig. 2. The wind turbine has been connected to a permanent magnet synchronous generator (PMSG) whose output has been given to a rectifier. Rectified voltage is fed to the DC-DC boost converter for power exchange between a wind turbine and the DC bus. This converter consists of an inductor L_w with a series resistance R_w, an insulated gate bipolar transistor (IGBT) switch S_1, a diode D_1 and a capacitor C_w at the output for filtering.

2.2. PV energy system

A solar panel is made up of PV modules consisting of cells that absorb sunlight and convert it into direct current (DC). The configuration of the PV energy system has been shown in Fig. 2. The PV array has been connected to a DC-DC buck-boost converter for power exchange with the DC bus which has been assumed to be operating in continuous conduction mode (CCM). There are two modes of operation of the buck-boost converter. In the first mode, both the switches S_2 and $\bar{S_2}$ are closed/ON and both the diodes D_2 and D_3 are open/OFF. In this mode, the load is disconnected from the source and the inductor gets charged. In the second mode, both switches are open/OFF and both diodes are closed/ON. In this mode, the inductor gets discharged by connecting to the load. This converter consists of two capacitors: C_{pv} at the input and C_{pout} at the output, two IGBT switches S_2 and $\bar{S_2}$ and two diodes D_2 and D_3.

2.3. Energy storage system

The energy storage system (ESS) consists of a battery and a SC. Battery discharges and charges itself under varying load conditions along with RESS. SC provides instant power during peaks of the load and has been used to supply transient power. The configuration of ESS has been shown in Fig. 2. The battery has been connected to the DC bus through bi-directional DC-DC buck-boost converter for bi-directional flow of current depending upon the load demands and SoC of the battery. It consists of an inductor L_{bat} with series resistance R_{bat}, two IGBT switches S_3 and S_4, and an output filter capacitor C_{DC}. SC has been attached to the DC bus through a DC-DC bidirectional buck-boost converter for power regulation which includes inductor L_{sc} with series resistance R_{sc} and two IGBT switches S_5 and S_6. When S_3 is ON and S_4 is OFF, it acts as a boost converter and battery discharges. When S_3 is OFF and S_4 is ON, it acts as a buck converter and battery charges. Similarly, when S_5 is ON and S_6 is OFF, it acts as a boost converter and SC discharges. When S_5 is OFF and S_6 is ON, it acts as a buck converter and SC charges.

3. Mathematical model of DC microgrid

The mathematical model of the RESs and ESS has been presented by combining the currents and voltages of the individual systems presented in Sections 2.1–2.3 to form a DC MG under consideration. The average state-space model of the converters employed in this work can be expressed by the following equations:

$$\dot{q_1} = \frac{V_{in}}{L_w} - \frac{R_w}{L_w}q_1 - (1-u_1)\frac{q_2}{L_w} \tag{1}$$

$$\dot{q_2} = (1-u_1)\frac{q_1}{C_w} - \frac{q_2}{R_w C_w} \tag{2}$$

$$\dot{q_3} = \frac{I_{pv}}{C_{pv}} - u_2\frac{q_4}{C_{pv}} \tag{3}$$

$$\dot{q_4} = u_2\frac{q_3}{L_{pv}} + u_2\frac{q_5}{L_{pv}} - \frac{q_5}{L_{pv}} \tag{4}$$

$$\dot{q_5} = (1-u_2)\frac{q_4}{C_{pout}} - \frac{I_{pv}}{C_{pout}} \tag{5}$$

$$\dot{q_6} = \frac{V_b}{L_b} - \frac{R_b}{L_b}q_6 - u_{34}\frac{q_8}{L_b} \tag{6}$$

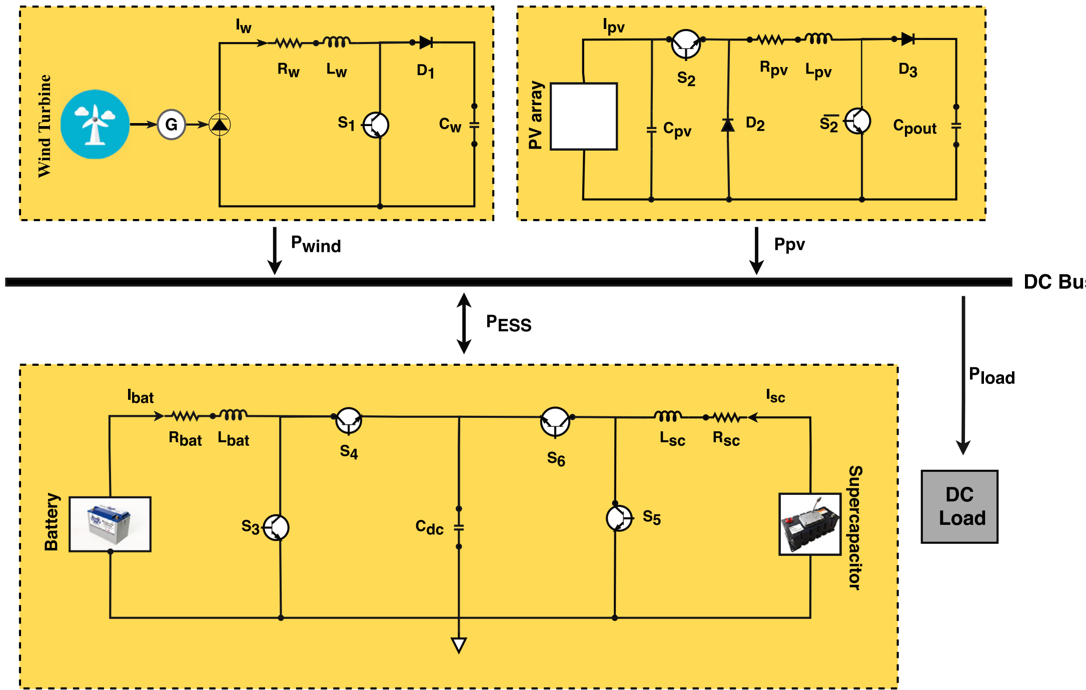

Fig. 2. Block diagram of components integrated to form a DC microgrid.

$$\dot{q}_7 = \frac{V_{sc}}{L_{sc}} - \frac{R_{sc}}{L_{sc}} q_7 - u_{56} \frac{q_8}{L_{sc}} \tag{7}$$

$$\dot{q}_8 = u_{34} \frac{q_6}{C_{DC}} + \frac{I_{ESS}}{C_{DC}} - u_{56} \frac{q_7}{C_{DC}} \tag{8}$$

where q_1 and q_2 represent the state-space model for wind energy system, q_3, q_4 and q_5 represent the state-space model for PV energy system and q_6, q_7 and q_8 represent the state-space model for ESS.

In Eqs. (1)–(8), q_1 is wind current I_w, q_2 is output voltage V_w, q_3 is input voltage of PV array V_{pv}, q_4 is PV current I_l, q_5 is output voltage of PV V_{pout}, q_6 is battery current I_b, q_7 is SC current I_{sc} and q_8 is DC bus voltage V_{DC}. Similarly, u_1, u_2, u_{34} and u_{56} are the control inputs of the system.

4. System analysis

To understand the behavior of the system, a complete analysis has been conducted to analyze the design of the controller required for the control of DC microgrid as given:

- **Dynamical behavior:** As the presented approach is rich of DC-DC power converters, it gives rise to a variety of nonlinear dynamics due to power sources and electromagnetic interactions between them as well as the switching phenomena. Furthermore, the nonlinear behavior exhibited by the converters has been divided into chaos and bifurcation [34]. To avoid chaos in the circuits, average-state space model of the system has been presented to be useful whereas, Lyapunov stability analysis proves to be beneficial in terms of avoiding bifurcation.
- **Nonlinear nature:** The connection, interaction between the power sources and switching of the converters make the system highly nonlinear. It has been figured out that nonlinearity of the converters can be well-handled by the Lyapunov-based schemes which provide satisfactory performance in terms of sensitivity, robustness and improved transient response [35].
- **Non-minimal phase behavior:** This type of behavior is exhibited by the inductor in the circuit when the current lags the reference signal which occurs in boost and buck-boost converters [34]. To avoid this behavior, current-based control approaches are employed which force the currents to follow their respective references using an indirect control approach.

The aforementioned issues lead to the design of a nonlinear controller which can cater for the nonlinear dynamic behavior of the power converters. Moreover, the parameters of the proposed STSMC-based nonlinear controller are designed in the next section in such a way that it adjusts the nonlinearities that arise with the use of power electronics and switching phenomena.

5. Design of nonlinear controllers and energy management system

To eliminate the problems faced during the control of DC-DC power converters as explained in the previous section of system analysis, STSMC-based decentralized nonlinear controllers have been designed for the wind and PV energy systems with an energy storage system as shown in Fig. 3. SMC is known for displaying less sensitivity to the extrinsic variations and disturbances. An energy management system based on fuzzy logic has been proposed in the following subsection for sharing of load demands between RESs and ESS. The objectives of the designed framework are as follows:

(1) MPPT of wind and PV energy systems to have maximum power from RESs,
(2) The tracking of the state currents of battery and SC to their reference values to reduce overall dependency on RESs,
(3) Voltage regulation of microgrid's DC bus to its desired value through energy management system to ensure power sharing between DG units and load,
(4) System's global asymptotic stability.

As STSMC involves higher degree of the derivatives of the sliding surface, it outperforms the first-order sliding mode controllers in

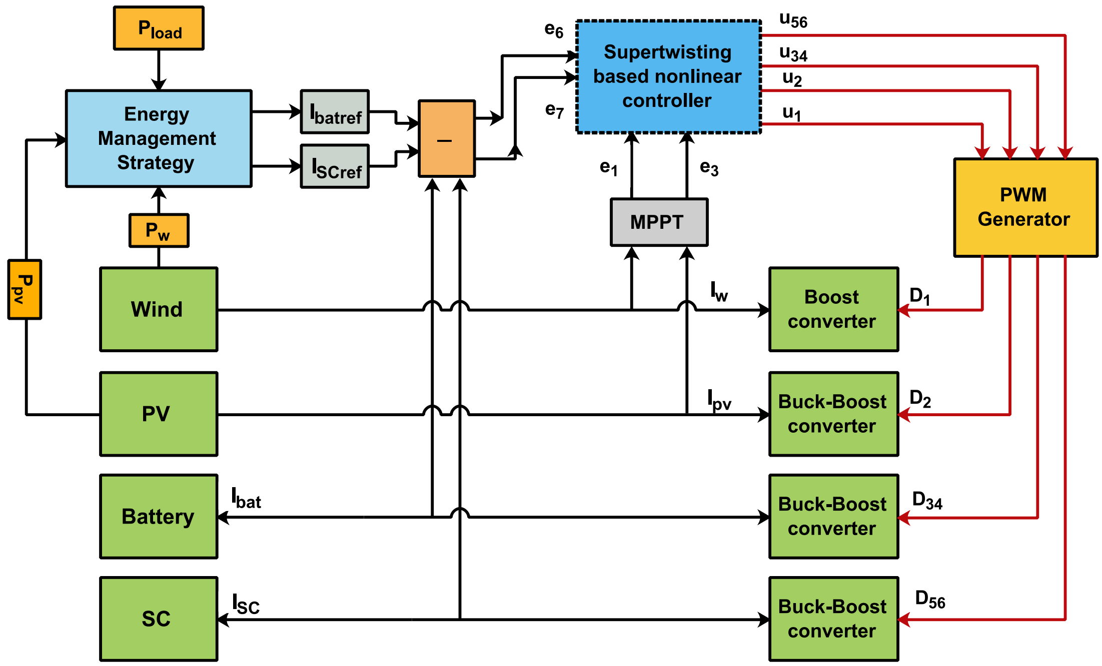

Fig. 3. Control design for DC microgrid.

terms of robustness to disturbance variations and reduction in the chattering of the sliding surface. This technique converges the sliding surface S as well as its derivative $\dot{S}$ to zero during finite time.

5.1. Controller design for wind energy system

The processing of converting energy from wind turbine into electricity involves the conversion of the kinetic energy into electrical energy. As the wind speed changes, the speed of shaft and power captured by it also changes. To obtain maximum power all the time, the wind energy system has to be operated at its maximum power point. Optimal torque control (OTC) technique has been used for the MPPT as it does not load additional stress on the DC-link capacitor, turbine blades as well as the pitch angle controller [36]. The reference wind current generated at MPP from OTC technique is expressed as:

$$I_{ref} = \frac{t_{m-ref} \times w_m}{v_d} \tag{9}$$

where, v_d is the rectified voltage from PMSG, w_m is the shaft speed and t_{m-ref} is the maximum reference torque of the wind turbine under optimum conditions expressed as:

$$T_{m-ref} = 0.5\rho r^5 \pi \frac{c_{p-max}}{\lambda_{opt}^3} {w_m}^2 \tag{10}$$

where, ρ (kg/m^3) express the density of the air, r(m) is the turbine radius, c_{p-max} is the maximum power coefficient of wind turbine, λ_{opt} is optimum tip speed ratio which depends on the shaft speed w_m(m/s).

In order to track the wind current state q_1 to its desired state value q_{1ref} to have maximum power generation from this RES, we define an error term for the design of the its controller as follows:

$$e_1 = q_1 - q_{1ref} \tag{11}$$

where q_{1ref} is the reference wind current I_{ref}. To design a supertwisting sliding mode controller, a sliding surface has been selected which facilitates the system to reach the sliding surface to attain the desired reference value. As the state space model of the wind energy system has one control input, so the sliding surface has been selected as follows:

$$S_1 = a_1 e_1 \tag{12}$$

where a_1 is one of the design parameter of the sliding surface having positive constant value. Taking time derivative of Eq. (12) gives:

$$\dot{S_1} = a_1 \dot{e_1} \tag{13}$$

The time derivative of Eq. (11) yields the following equation:

$$\dot{e_1} = \dot{q_1} - \dot{q}_{1ref} \tag{14}$$

Replacing the value of $\dot{q_1}$ from Eq. (1) in Eq. (14) gives:

$$\dot{e_1} = \frac{V_{in}}{L_w} - \frac{R_w}{L_w} q_1 - (1-u_1)\frac{q_2}{L_w} - \dot{q}_{1ref} \tag{15}$$

Substituting the value of $\dot{e_1}$ from Eq. (15) in Eq. (13) gives:

$$\dot{S_1} = a_1\left[\frac{V_{in}}{L_w} - \frac{R_w}{L_w} q_1 - (1-u_1)\frac{q_2}{L_w} - \dot{q}_{1ref}\right] \tag{16}$$

The control law u_1 has been chosen in such a way that it brings the system towards the global asymptotic stability expressed as:

$$u_1 = u_{nm1} + u_{sw1} \tag{17}$$

where u_{sw1} is the supertwisting algorithm representing the switching control which is responsible for keeping the trajectory on the sliding surface and u_{nm1} represents the nominal control which is responsible for bringing the state trajectory to the sliding surface. Putting $\dot{S_1} = 0$ for finding the value of u_{nm1} gives:

$$u_{nm1} = 1 + \frac{L_w}{a_1 q_2}\left(-\frac{a_1 V_{in}}{L_w} + \frac{a_1 R_w}{L_w} q_1 + a_1 \dot{q}_{1ref}\right) \tag{18}$$

and

$$u_{sw1} = \frac{L_w}{a_1 q_2}\left(-k_1 \, |S_1|^{\alpha} \, sgn\,(\frac{S_1}{\phi_1}) - k_2 \int sgn\,(\frac{S_1}{\phi_1})\, dt\right) \tag{19}$$

In Eq. (19), α is a constant having value between 0 and 1 which converges the system to the sliding surface, constants k_1 and k_2

are positive gains used to adjust the tracking of STSMC controller, ϕ_1 is the degree of nonlinearity used to reduce the chattering effect and sgn represents Signum function which is given as follows:

$$Sgn\,(S) = \begin{cases} -1 & if \quad S < 0 \\ 0 & if \quad S = 0 \\ 1 & if \quad S > 0 \end{cases} \tag{20}$$

Substituting the value of u_1 using Eqs. (17), (18), (19) in Eq. (16) yields the following result:

$$\dot{S_1} = -k_1\,|S_1|^{\alpha}\,sgn\,(\frac{S_1}{\phi_1}) - k_2 \int sgn\,(\frac{S_1}{\phi_1})\,dt \tag{21}$$

Rearranging Eq. (21) in the following form for stability analysis:

$$\dot{S_1} = w_1 + z_1 \tag{22}$$

where,

$$w_1 = -k_1\,|S_1|^{\alpha}\,sgn\,(\frac{S_1}{\phi_1}) \tag{23}$$

$$\dot{z_1} = -k_2\,sgn\,(\frac{S_1}{\phi_1}) \tag{24}$$

The following Lyapunov candidate function has been used to evaluate the stability analysis of the system:

$$V_1 = 2\,k_2\,|S_1| + \frac{1}{2}z_1^2 + \frac{1}{2}\left(k_1|S_1|^{\alpha}\,sgn\,(\frac{S_1}{\phi_1}) - z_1\right)^2 \tag{25}$$

The Lyapunov function in Eq. (25) can be written in a quadratic form $V_1 = x_1^T P_1 x_1$ where:

$$x_1^T = \left[|S_1|^{\alpha}\,sgn\,(\frac{S_1}{\phi_1}) \quad z_1 \right] \tag{26}$$

$$P_1 = \frac{1}{2}\begin{bmatrix} 4k_2 + k_1^2 & -k_1 \\ -k_1 & 2 \end{bmatrix} \tag{27}$$

where k_1 and k_2 are positive constants of P_1 matrix which is positive definite. The stability analysis of the system using methods presented in [37] and [38] deduce that the proposed controller u_1 meets the Lyapunov stability criterion as shown by Eq. (28) which ensures the finite time convergence of error to zero. It also depicts that the wind energy system is able to produce maximum power throughout the day.

$$\dot{V_1} \leq 0 \tag{28}$$

5.2. Controller design for PV energy system

PV module converts the solar energy into electrical energy without producing any pollution. Many modules combine to form a PV array whose conversion efficiency depends on environmental parameters i.e. irradiance and temperature. The duty cycle of the DC-DC buck-boost converter connected with the PV array, as shown in Fig. 3, has been varied in such a way that the PV array always operates at its maximum power point. Neural network based MPPT provides more accurate results than the conventional perturb and observe based MPPT algorithm in less time [39]. Due to solar energy's intermittent nature, a neural network has been optimized to generate the maximum peak power voltage V_{MPP} reference at which PV array has been operated.

Over time, variations in weather conditions such as fog, heat, dust, and other particles floating in the air cover the panel which drastically decreases the efficiency of the PV system's power conversion process. As the values generated by neural network closely match the target values, it can be used for the prediction of future indicator values of V_{MPP} based on past data and trend recognition of irradiance and temperature irrespective of the conditions aforementioned.

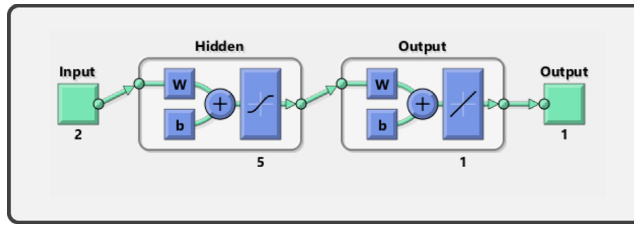

Fig. 4. Neural network structure for MPPT.

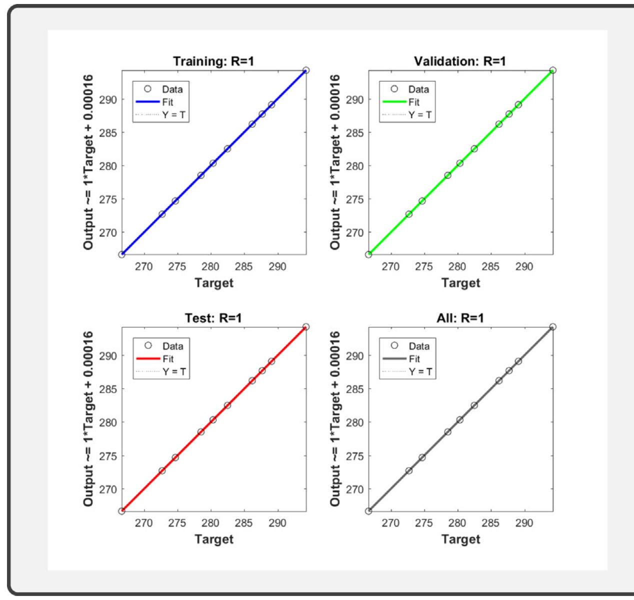

Fig. 5. Regression plot.

The data on which neural network has been trained and given as target is taken from the Simulink model of PV array with varying temperature and irradiance data points. The neural network presented in this paper consists of two inputs, i.e. temperature and solar irradiance and one output i.e. V_{MPP} as shown in Fig. 4. The performance of the network has been controlled by the number of neurons in the hidden layer. The input data has been provided to the hidden layers where output data calculation has been performed.

To train the neural network, the Levenberg–Marquardt algorithm has been implemented for solving problems exhibiting a nonlinear nature i.e. the variations in irradiance and temperature. From the regression plot generated using neural network toolbox in MATLAB® (2019a) shown in Fig. 5, it can be observed that the output value of V_{MPP} matches the target data accurately. In regression plot, the solid line represents the perfect correlation between predicted and target data and the dashed line represents the best fit produced by the neural network algorithm. A comparison of target values of V_{MPP} and values generated by the neural network has been done in Table 1.

In order to track the PV array voltage state q_3 to its desired state value q_{3ref} to have maximum power generation from this RES, we define error term for designing of the PV energy system controller as follows:

$$e_3 = q_3 - q_{3ref} \tag{29}$$

Table 1
Comparison of V_{MPP}.

Irr. (W/m^2)	Temp. (C)	V_{mpp} Actual (V)	V_{mpp} NN (V)
640	21	294.2532	293.3854
700	26	287.6810	286.1634
800	31.6	280.3080	281.6295
900	37.4	272.6730	270.9442
1000	42	266.6100	266.7132
855	36	274.6547	273.4962
740	33	278.4962	278.0692
615	30	282.4724	281.9110
515	27.2	286.1774	287.3858
445	25	289.0853	288.2193

As the state space model of PV energy system has only one control input, so only one sliding surface has been selected as follows:

$$S_3 = a_3 e_3 \tag{30}$$

where a_3 is a design parameter of the sliding surface having positive constant value. Taking time derivative of Eq. (30) gives:

$$\dot{S_3} = a_3 \dot{e_3} \tag{31}$$

The time derivative of Eq. (29) yields the following equation:

$$\dot{e_3} = \dot{q_3} - \dot{q}_{3ref} \tag{32}$$

Replacing the value of $\dot{q_3}$ from Eq. (3) in Eq. (32) gives:

$$\dot{e_3} = \frac{I_{pv}}{C_{pv}} - u_2 \frac{q_4}{C_{pv}} - \dot{q}_{3ref} \tag{33}$$

Substituting $\dot{e_3}$ from Eq. (33) in Eq. (31) gives:

$$\dot{S_3} = a_3 \left[\frac{I_{pv}}{C_{pv}} - u_2 \frac{q_4}{C_{pv}} - \dot{q}_{3ref} \right] \tag{34}$$

The control law u_2 for the asymptotic stability can be given as:

$$u_2 = u_{nm2} + u_{sw2} \tag{35}$$

Putting $\dot{S_3} = 0$ for finding the value of u_{nm2} gives:

$$u_{nm2} = \frac{C_{pv}}{a_3 q_4} \left(\frac{a_3 I_{pv}}{C_{pv}} - a_3 \dot{q}_{3ref} \right) \tag{36}$$

where u_{nm2} represents the nominal control which is responsible for bringing the state trajectory to the sliding surface and,

$$u_{sw2} = \frac{C_{pv}}{a_3 q_4} \left(k_3 \, |S_3|^{\beta} \, sgn\,(\frac{S_3}{\phi_3}) + k_4 \int sgn\,(\frac{S_3}{\phi_3})\, dt \right) \tag{37}$$

u_{sw2} is the supertwisting algorithm representing the switching control which is responsible for keeping the trajectory on the sliding surface. β is constant having value between 0 and 1 which converges the system to the sliding surface, constants k_3 and k_4 are positive gains used to adjust the tracking of STSMC controller and ϕ_3 is the degree of nonlinearity used to minimize the chattering effect.

Substituting the value of u_2 using Eqs. (35), (36), (37) in Eq. (34) yields the following result:

$$\dot{S_3} = -k_3 \, |S_3|^{\beta} \, sgn\,(\frac{S_3}{\phi_3}) - k_4 \int sgn\,(\frac{S_3}{\phi_3})\, dt \tag{38}$$

For the stability analysis, Eq. (38) has been rearranged as follows:

$$\dot{S_3} = w_3 + z_3 \tag{39}$$

where,

$$w_3 = -k_3 \, |S_3|^{\beta} \, sgn\,(\frac{S_3}{\phi_3}) \tag{40}$$

$$\dot{z_3} = -k_4 \, sgn\,(\frac{S_3}{\phi_3}) \tag{41}$$

To evaluate the stability analysis of the system, the following steps have been conducted:

$$V_3 = 2\,k_4\,|S_3| + \frac{1}{2} z_3^2 + \frac{1}{2} \left(k_3 |S_3|^{\beta} \, sgn\,(\frac{S_3}{\phi_3}) - z_3 \right)^2 \tag{42}$$

The Lyapunov function in Eq. (42) can be written in a quadratic form $V_3 = x_3^T P_3 x_3$ where:

$$x_3^T = \begin{bmatrix} |S_3|^{\beta} \, sgn\,(\frac{S_3}{\phi_3}) & z_3 \end{bmatrix} \tag{43}$$

$$P_3 = \frac{1}{2} \begin{bmatrix} 4k_4 + k_3^2 & -k_3 \\ -k_3 & 2 \end{bmatrix} \tag{44}$$

In Eq. (44), k_3 and k_4 are positive constants of positive definite matrix P_3. The Lyapunov stability analysis of the system has been conducted by performing the same procedure as discussed in previous section and it has been inferred through Eq. (45) that the chosen control law u_2 meets the Lyapunov stability criterion as it ensures the finite time convergence of error to zero. It also depicts that the PV energy system is able to produce maximum power in spite of varying environmental conditions.

$$\dot{V_3} \le 0 \tag{45}$$

5.3. Fuzzy logic based energy management system

Since the irradiance, temperature and wind speed vary throughout the day, the power generated from RESs varies. To meet the load demand, an energy management system (EMS) is essential. For this purpose, a fuzzy logic based EMS has been designed as it provides a better way to deal with uncertainty through linguistic variables and logic inferential rules. In fuzzy logic, the input is provided as a set of crisp values. A fuzzifier translates the crisp values into its corresponding membership values in membership functions. Rule base knowledge is formulated to obtain the fuzzy output and to have a crisp output, a defuzzifier is employed [40].

The proposed EMS has been implemented on MATLAB® (2019a) using Fuzzy Logic Designer and Mamdani Fuzzy Inference System (FIS) as illustrated in Fig. 6. It consists of 3 inputs, 1 output and 18 rules which have been formulated on the energy management algorithm presented in [11]. Sample of rules designed for this energy management system, shown in Table 2, are intuition-based and have been validated through simulations. The input and output parameters with their respective membership functions have been implemented in FIS as follows:

(1) **Input 1: Power Balance**
Power balance refers to the power in DC MG that must be balanced under variable power generation from RESs and load demand conditions and has been calculated as follows:

$$P_B = P_{load} - P_w - P_{PV} \tag{46}$$

Power balance input has two membership functions Less than Zero (LZ) and Greater than Zero (GZ). The range of this parameter depicts the power balance in terms of −20kW to 20kW as displayed in Fig. 7.

(2) **Input 2: SoC of Battery**
SoC of battery can be calculated as follows:

$$SoC_{Battery} = SoC_{Binitial} - \frac{1}{3600 C_N} \int q_6 dt \tag{47}$$

where $SoC_{Binitial}$ refers to the SoC of battery at $t = 0$ s, C_N refers to the nominal capacity of battery and q_6 is the

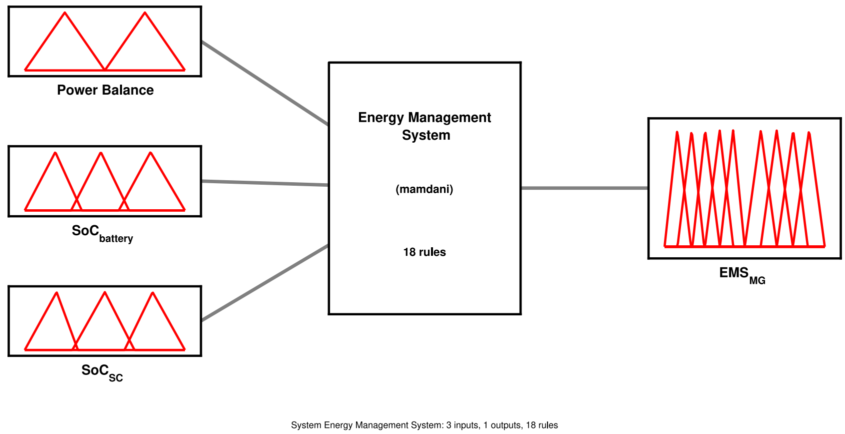

Fig. 6. FIS for energy management system.

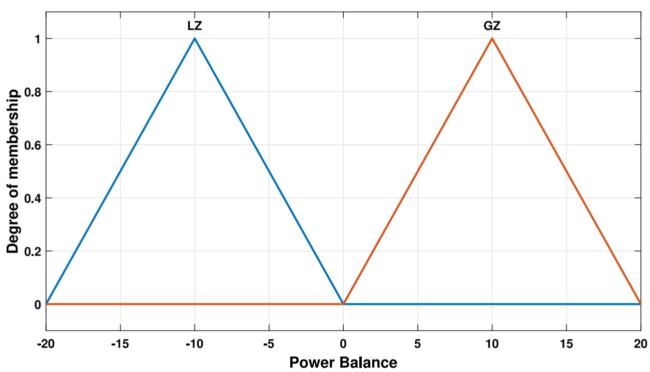

Fig. 7. Membership functions of power balance.

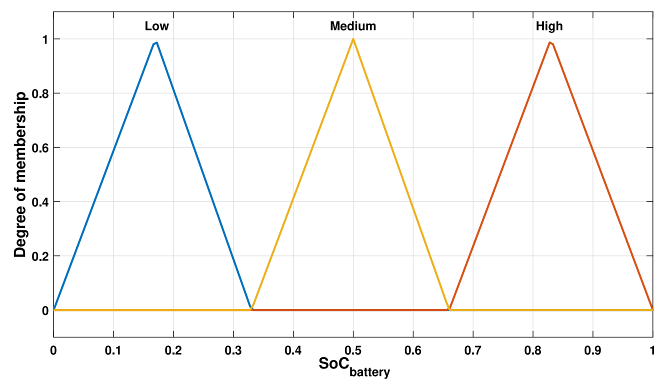

Fig. 8. Membership functions of battery SoC.

battery current. Battery SoC has three membership functions *Low*, *Medium* and *High*. The range of this parameter depicts the battery SoC % which can lie between 0 to 100% as displayed in Fig. 8.

(3) **Input 3: SoC of SC**

SoC of SC can be calculated as follows:

$$SoC_{SC} = SoC_{SCinitial} - \frac{1}{3600C_N}\int q_7 dt \tag{48}$$

where $SoC_{SCinitial}$ refers to the SoC of SC at $t = 0$ s, C_N refers to the nominal capacity of SC and q_7 is the SC current. SoC of SC has three membership functions *Low*, *Medium* and *High*. The range of this parameter depicts the SC SoC % which can lie between 0 to 100% displayed in Fig. 9.

(4) **Output: Power distribution among energy sources**

The output from EMS_{MG} will decide the power distribution among all the sources depending upon the power balance, SoC of battery and SC. It has nine membership functions as displayed in Fig. 10. If P_B is negative and SoC of both the battery and the SC are high, then wind and PV energy systems are operated in off MPPT mode as load power requirement is less. If P_B is positive and SoC of battery and SC are not low, then both will discharge. If SoC of either battery or SC is low, it does not operate and in the worst-case scenario when SoC of both sources is low, load shedding occurs to maintain power balance.

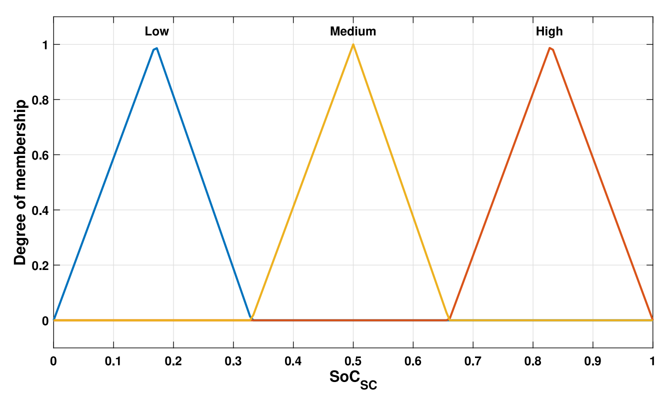

Fig. 9. Membership functions of SC SoC.

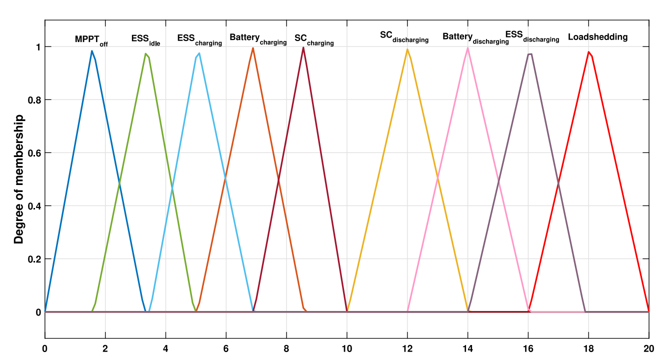

Fig. 10. Membership functions of output.

Table 2
Sample of designed fuzzy inferential rules.

Rule no.	P_B	SoC_{Bat}	SoC_{SC}	Output
1.	LZ	Low	Low	$ESS_{charging}$
2.	LZ	Low	Medium	$Battery_{charging}$
3.	LZ	Medium	Low	$SC_{charging}$
4.	LZ	High	High	$MPPT_{off}$
5.	LZ	Medium	Medium	ESS_{idle}
6.	GZ	High	High	$ESS_{discharging}$
7.	GZ	High	Low	$Battery_{discharging}$
8.	GZ	Low	High	$SC_{discharging}$
9.	GZ	Low	Low	Loadshedding

5.4. Controller design for ESS

To complement the power provided by RESs, ESS has been integrated to support and manage the load requirements connected with the DC MG. The integration of ESS with DC bus has been illustrated in Fig. 3. DC bus voltage V_{DC} cannot be regulated directly to V_{DCref} due to non-minimum phase behavior of buck-boost converter [41]. An indirect approach has been implemented in this paper in which V_{DC} has been regulated to V_{DCref} by the tracking of battery current I_b to its reference I_{batref}. The relationship between V_{DC} and I_b has been be explained as follows:

$$P_{in} = P_{out}$$

$$I_{batref} V_{bat} + I_{scref} V_{sc} = V_{DCref} I_{ESS} \tag{49}$$

where P_{bat}, P_{sc} and P_{load} denote battery power, SC power and output power respectively and I_{ESS} represents the output current from ESS. Denoting I_{batref} and I_{scref} as q_{6ref} and q_{7ref} respectively and solving Eq. (49) for q_{6ref}, the following expression has been obtained:

$$q_{6ref} = \varphi\left(\frac{q_{8ref} I_{ESS} - V_{sc} q_{7ref}}{v_{bat}}\right) \tag{50}$$

where φ represents different power losses of the converter which occurs due to resistances, inductances and switching. In ideal conditions, φ is 1 but the efficiency of power converter is not 100%, so the value of φ is always greater than 1.

To track the battery and SC currents to their desired state values q_{6ref} and q_{7ref} in order to share the load requirements with RESs, error terms have been defined as follows:

$$e_6 = q_6 - q_{6ref} \tag{51}$$

and,

$$e_7 = q_7 - q_{7ref} \tag{52}$$

Sliding surfaces for the design of controllers have been selected as:

$$S_6 = a_6 e_6 \tag{53}$$

and,

$$S_7 = a_7 e_7 \tag{54}$$

where a_6 and a_7 are the positive constant design parameters of the sliding surfaces. Taking time derivatives of Eqs. (53) and (54), we obtain:

$$\dot{S_6} = a_6 \dot{e_6} \tag{55}$$

and,

$$\dot{S_7} = a_7 \dot{e_7} \tag{56}$$

The time derivatives of Eqs. (51) and (52) yield the following equations:

$$\dot{e_6} = \dot{q_6} - \dot{q}_{6ref} \tag{57}$$

and,

$$\dot{e_7} = \dot{q_7} - \dot{q}_{7ref} \tag{58}$$

Replacing the values of $\dot{q_6}$ and $\dot{q_7}$ from Eqs. (6) and (7) in Eqs. (57) and (58), we get:

$$\dot{e_6} = \frac{V_b}{L_b} - \frac{R_b}{L_b} q_6 - u_{34}\frac{q_8}{L_b} - \dot{q}_{6ref} \tag{59}$$

and,

$$\dot{e_7} = \frac{V_{sc}}{L_{sc}} - \frac{R_{sc}}{L_{sc}} q_7 - u_{56}\frac{q_8}{L_{sc}} - \dot{q}_{7ref} \tag{60}$$

Substituting the respective values of $\dot{e_6}$ and $\dot{e_7}$ from Eqs. (59) and (60) in Eqs. (55) and (56) results in:

$$\dot{S_6} = a_6\left[\frac{V_b}{L_b} - \frac{R_b}{L_b} q_6 - u_{34}\frac{q_8}{L_b} - \dot{q}_{6ref}\right] \tag{61}$$

and,

$$\dot{S_7} = a_7\left[\frac{V_{sc}}{L_{sc}} - \frac{R_{sc}}{L_{sc}} q_7 - u_{56}\frac{q_8}{L_{sc}} - \dot{q}_{7ref}\right] \tag{62}$$

The control laws u_{34} and u_{56} which have been selected for the asymptotic stability of the system can be expressed as:

$$u_{34} = u_{nm34} + u_{sw34} \tag{63}$$

$$u_{56} = u_{nm56} + u_{sw56} \tag{64}$$

Putting $\dot{S_6} = 0$ for finding the value of u_{nm34} gives:

$$u_{nm34} = \frac{L_b}{a_6 q_8}\left(\frac{a_6 V_b}{L_b} - \frac{a_6 R_b}{L_b} q_6 - a_6 \dot{q}_{6ref}\right) \tag{65}$$

Placing $\dot{S_7} = 0$ for finding the value of u_{nm56} gives:

$$u_{nm56} = \frac{L_{sc}}{a_7 q_8}\left(\frac{a_7 V_{sc}}{L_{sc}} - \frac{a_7 R_{sc}}{L_{sc}} q_7 - a_7 \dot{q}_{7ref}\right) \tag{66}$$

where u_{nm34} and u_{nm56} represent the nominal controls which are responsible for bringing the state trajectories to the sliding surfaces and,

$$u_{sw34} = \frac{L_b}{a_6 q_8}\left(k_6\, |S_6|^{\zeta}\, sgn\left(\frac{S_6}{\phi_6}\right) + k_7 \int sgn\left(\frac{S_6}{\phi_6}\right) dt\right) \tag{67}$$

$$u_{sw56} = \frac{L_{sc}}{a_7 q_8}\left(k_8\, |S_7|^{\gamma}\, sgn\left(\frac{S_7}{\phi_7}\right) + k_9 \int sgn\left(\frac{S_7}{\phi_7}\right) dt\right) \tag{68}$$

u_{sw34} and u_{sw56} are based on the supertwisting algorithm representing the switching controls which are responsible for keeping the trajectories on the sliding surfaces. ζ and γ are constants having values between 0 and 1 which converge the system to the sliding surface, constants k_6, k_7, k_8 and k_9 are positive gains used to adjust the tracking of STSMC controller and ϕ_6, ϕ_7 are degree of nonlinearity used to minimize the chattering effect.

Substituting the values of u_{34} and u_{56} using Eqs. (63), (64) in Eqs. (61), (62) respectively yield the following results:

$$\dot{S_6} = \left(-k_6\, |S_6|^{\zeta}\, sgn\left(\frac{S_6}{\phi_6}\right) - k_7 \int sgn\left(\frac{S_6}{\phi_6}\right) dt\right) \tag{69}$$

$$\dot{S_7} = \left(-k_8\, |S_7|^{\gamma}\, sgn\left(\frac{S_7}{\phi_7}\right) - k_9 \int sgn\left(\frac{S_7}{\phi_7}\right) dt\right) \tag{70}$$

Rearranging Eqs. (69), (70) in the following forms for stability analysis give:

$$\dot{S_6} = w_6 + z_6 \tag{71}$$

$$\dot{S_7} = w_7 + z_7 \tag{72}$$

where,

$$w_6 = -k_6\,|S_6|^{\zeta}\,sgn\,(\frac{S_6}{\phi_6}) \quad (73)$$

$$\dot{z_6} = -k_7\,sgn\,(\frac{S_6}{\phi_6}) \quad (74)$$

and,

$$w_7 = -k_8\,|S_7|^{\gamma}\,sgn\,(\frac{S_7}{\phi_7}) \quad (75)$$

$$\dot{z_7} = -k_9\,sgn\,(\frac{S_7}{\phi_7}) \quad (76)$$

The following Lyapunov candidate functions have been used to evaluate the stability analysis of the system:

$$V_6 = 2\,k_7\,|S_6| + \frac{1}{2}z_6^2 + \frac{1}{2}\left(k_6|S_6|^{\zeta}\,sgn\,(\frac{S_6}{\phi_6}) - z_6\right)^2 \quad (77)$$

$$V_7 = 2\,k_9\,|S_7| + \frac{1}{2}z_7^2 + \frac{1}{2}\left(k_8|S_7|^{\gamma}\,sgn\,(\frac{S_7}{\phi_7}) - z_7\right)^2 \quad (78)$$

The Lyapunov functions in Eqs. (77), (78) can be written in quadratic forms $V_6 = x_6^T P_6 x_6$ and $V_7 = x_7^T P_7 x_7$ where:

$$x_6^T = \begin{bmatrix} |S_6|^{\zeta}\,sgn\,(\frac{S_6}{\phi_6}) & z_6 \end{bmatrix} \quad (79)$$

$$P_6 = \frac{1}{2}\begin{bmatrix} 4k_7 + k_6^2 & -k_6 \\ -k_6 & 2 \end{bmatrix} \quad (80)$$

and,

$$x_7^T = \begin{bmatrix} |S_7|^{\gamma}\,sgn\,(\frac{S_7}{\phi_7}) & z_7 \end{bmatrix} \quad (81)$$

$$P_7 = \frac{1}{2}\begin{bmatrix} 4k_9 + k_8^2 & -k_8 \\ -k_8 & 2 \end{bmatrix} \quad (82)$$

In Eq. (80) and (82), P_6 and P_7 are positive definite matrices with the positive values of k_6, k_7, k_8 and k_9. By performing the stability analysis of Lyapunov functions as briefed in the previous sections, it can be concluded that the control laws u_{34} and u_{56} makes the system asymptotically stable as shown by Eqs. (83) and (84). These STSMC controllers ensure the effective power management between RESs and ESS and a stable DC MG operation under varying load conditions.

$$\dot{V_6} \leq 0 \quad (83)$$

$$\dot{V_7} \leq 0 \quad (84)$$

6. Simulation results and discussion

The main objective of the proposed controllers is the fulfillment of load demands by RESs and ESS maintaining the load-generation balance under varying load conditions. The proposed controller in Eq. (17) has been simulated on MATLAB/Simulink® (2019a) to verify the performance and tracking of wind current. It can be observed in Fig. 12 that the wind current depends on the wind speed as shown in Fig. 11. The tracking of the wind current reference by the proposed controller can be seen in Fig. 12 which ensures the maximum contribution from wind energy system.

The proposed controller in Eq. (35) has been simulated in the same environment to verify the performance and tracking of PV voltage. Fig. 13 shows the PV current generated against the reference voltage V_{pvref} which was obtained from neural network as mentioned in Table 1. In Fig. 14, the tracking of PV reference voltage by the proposed controller can be appreciated which ensures the maximum output power from PV modules under varying environmental conditions.

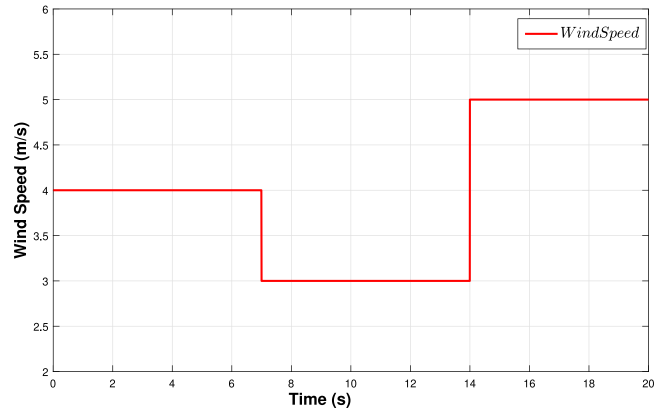

Fig. 11. Wind speed.

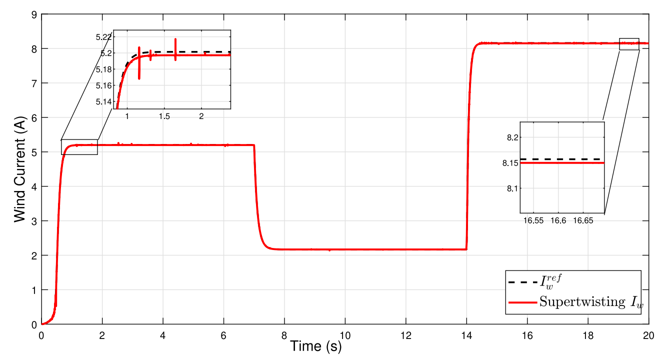

Fig. 12. State x_1: Wind current I_w.

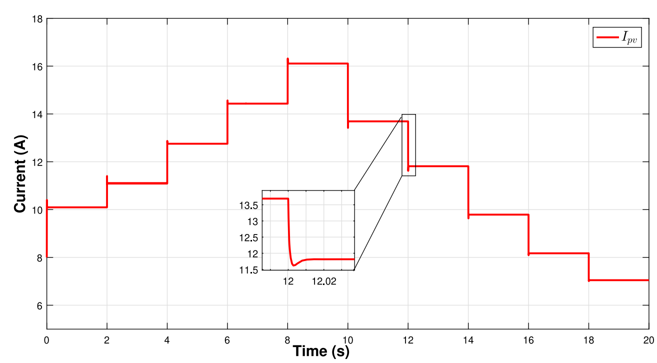

Fig. 13. PV current I_{pv}.

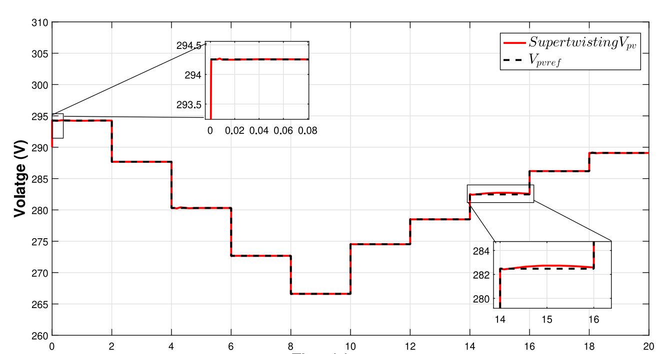

Fig. 14. State x_3: PV voltage V_{pv}.

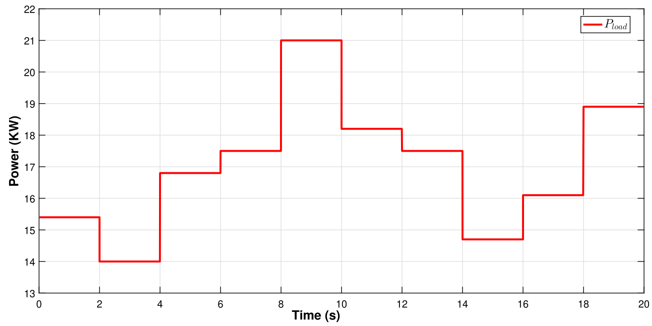

Fig. 15. Load power.

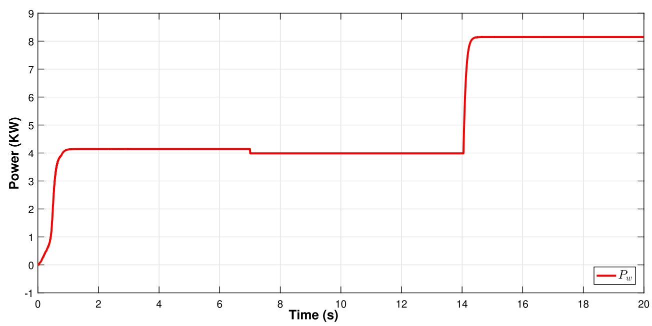

Fig. 16. Wind system power.

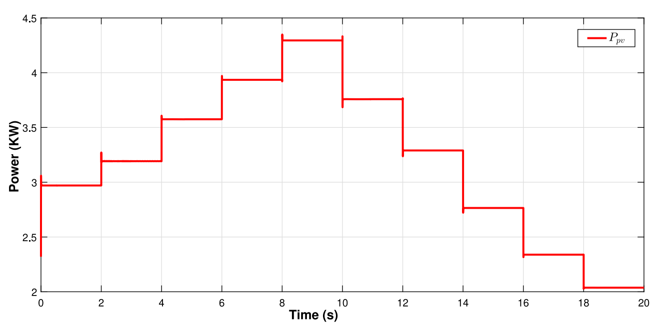

Fig. 17. PV system power.

The varying load power required to be supplied by the RESs and ESS has been shown in Fig. 15. The intermittent power generated by wind and PV system has been shown in Fig. 16 and Fig. 17 respectively. Resultant power shown in Fig. 18 is the power obtained from power balance Eq. (46) which needs to be supplied by the battery and SC depending on their SoC in this work. It should be noted here that without ESS to fulfill the remaining load demands, loadshedding would have been performed which shows the inefficient performance of the system.

A fuzzy logic controller (FLC) has been implemented in MATLAB/Simulink® (2019a) to verify the effectiveness of proposed EMS. It can be observed that the resultant power is greater than zero from $t = 0$ s to $t = 20$ s, therefore it lies in the Greater than Zero membership function of Fig. 7. The SoC of battery in Fig. 19 lies in the *High* membership function of Fig. 8 and the SoC of SC in Fig. 20 lies in the *High* membership function of Fig. 9. According to the rules demonstrated in Table 2, the output in the present case is $ESS_{discharging}$. In Fig. 21, the output of FLC from $t = 0$ s to $t = 20$ s is 16 which also lies in the $ESS_{discharging}$ membership function of Fig. 10 hence verifying the effective performance of the proposed EMS.

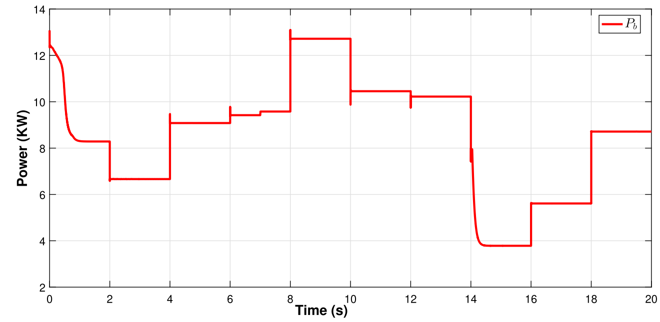

Fig. 18. Resultant power.

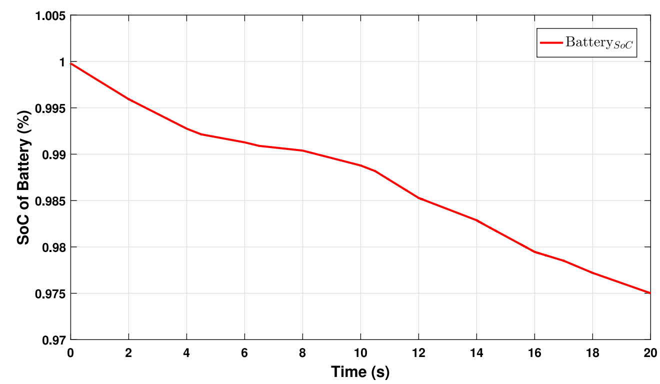

Fig. 19. Battery SoC.

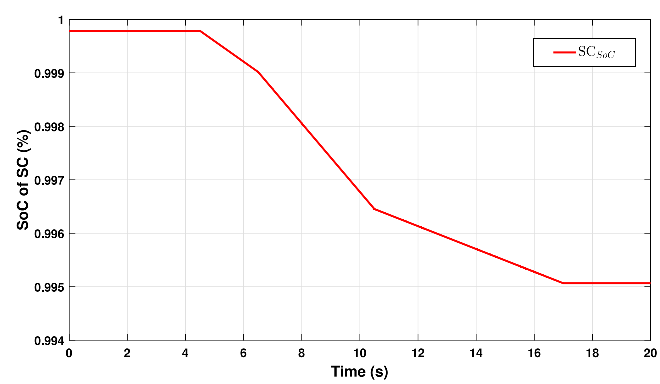

Fig. 20. SC SoC.

During low load conditions, the primary sources i.e. wind and PV energy system fulfill the power requirement by supplying the intermittent power generated shown in Figs. 16 and 17. During high load conditions as shown by the output of FLC, ESS provides the additional power with wind and PV energy systems to maintain the power balance between load and DC bus illustrated in Figs. 23 and 24.

The variable DC load current for which the controllers have been simulated, has been shown in Fig. 22. The proposed controllers in Eqs. (63) and (64) have also been simulated to verify the tracking of battery and SC currents during high load demands. The tracking of battery and SC current by the proposed controllers can be observed in Figs. 23 and 24 respectively. Battery reference current has been generated using control law given in Eq. (50). The sudden variations in battery reference current are due to the intermittent nature of wind and PV system as well as load variations.

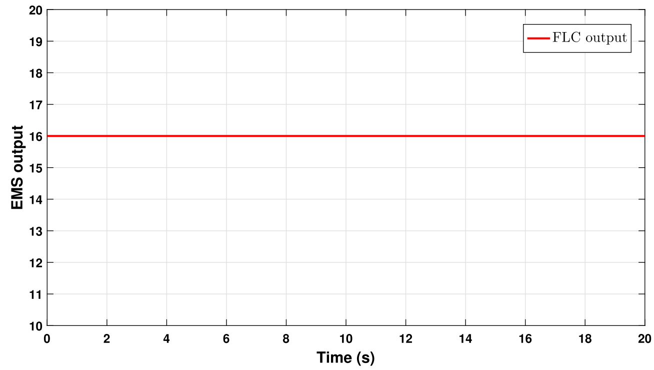

Fig. 21. FLC output.

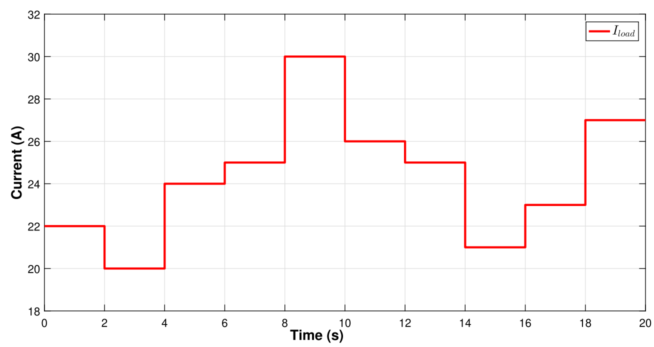

Fig. 22. DC load current.

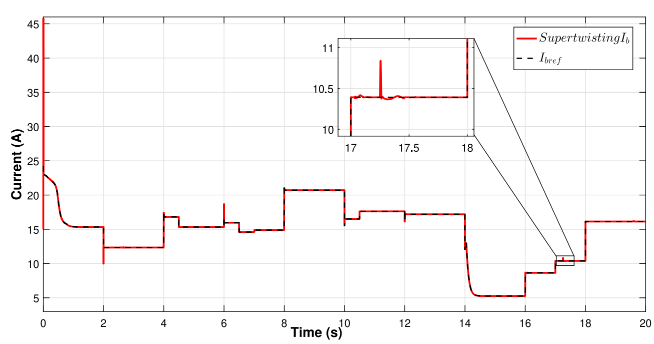

Fig. 23. State x_6: Battery current I_b.

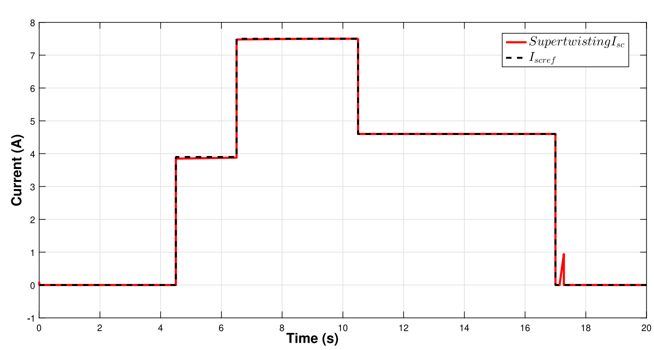

Fig. 24. State x_7: Supercapacitor current I_{sc}.

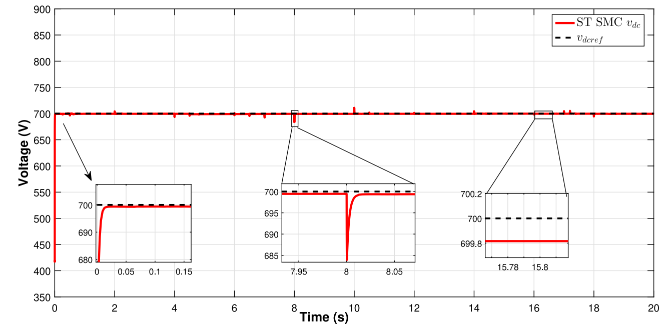

Fig. 25. State x_8: DC bus voltage V_{DC}.

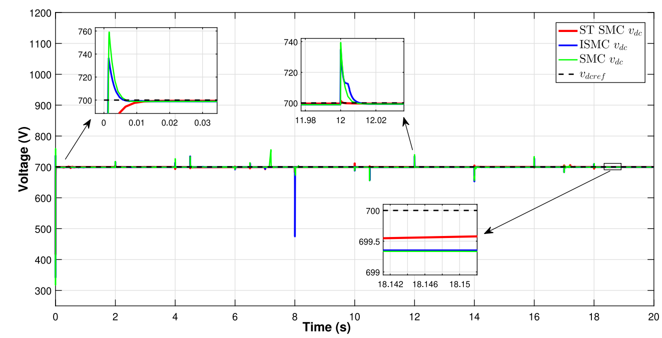

Fig. 26. Comparison of DC bus voltage (STSMC vs ISMC vs SMC).

From $t = 0$ s to $t = 4.5$ s, battery along with RESs fulfill the load requirements as SC stays idle. From $t = 4.5$ s to $t = 10$ s, SC supplies the additional power by discharging itself to share the load with battery and PV as the wind power decrease during this interval. From $t = 10$ s to $t = 14$ s, the load demand decreases but the intermittent power generated by RESs also reduce so battery along with SC fulfill the load requirement and from $t = 14$ s to $t = 20$ s, wind power increases as the wind speed increased, therefore, SC goes to idle mode during this period while battery and RESs fulfill the load requirements.

It can be observed in Fig. 25 that the proposed STSMC achieves the objective of DC bus voltage regulation despite the overshoots and undershoots which ensures the maximum power contribution from RESs as well as ESS. The tracking of the DC bus voltage to its reference value without any overshoot can be appreciated. One of the undershoots at $t = 8$ s has been shown in Fig. 25 with a peak voltage of 685 V but it is within the acceptable range of values as the DC bus voltage has been tracked all the time. The overshoots and undershoots are due to the changes in load demand and generated power.

The tracking of DC bus voltage to its desired reference with different control techniques has been shown in Fig. 26. It can be observed that STSMC achieves the steady state before $t = 0.01$ s while sliding mode control and integral sliding mode control (ISMC) display an overshoot with peak voltages of 740 V and 760 V respectively. Various overshoots and undershoots using SMC and ISMC can be observed and at $t = 12$ s, faster dynamic response of STSMC can be appreciated.

6.1. Hardware-in-the loop results

To validate the feasibility of the designed controllers, real-time controller hardware-in-the loop (C-HIL) experiment has been carried out as demonstrated in Fig. 27. C2000 Delfino™ with two MCU F28379D LaunchPads have been used which have TMS320F28379D dual core CPUs. The Launchpads operate at 200 MHz frequency. Moreover, the LaunchPads are linked to the MATLAB® with the TI C2000 Delfino™. The model of the plant has been simulated on MATLAB® Simulink environment and connected with the first LaunchPad. A closed loop is formed

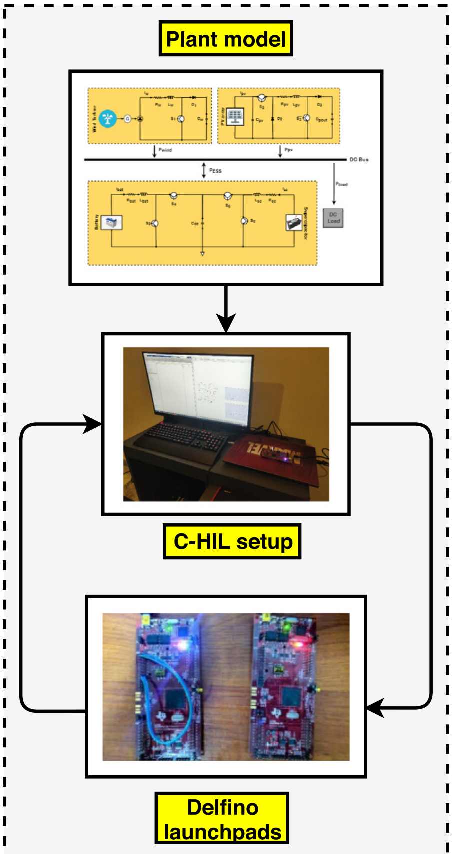

Fig. 27. Configuration of C-HIL.

between both of the LaunchPads as the controller burnt on the second LaunchPad generate the duty ratios which is given to the first LaunchPad on which the plant model is running. To facilitate the C-HIL experiments, a constant output power of wind and PV energy systems has been taken and they are operated at 3kW. C-HIL experiments have been conducted for two cases: constant load demand of 25 A and varying load demand. The results of the C-HIL experiments have been plotted in the same figure with the simulation results to evaluate the resemblance between them.

Figs. 28 and 29 display battery and SC currents respectively under constant load demand. It is worth noticing that the battery and SC both discharge simultaneously to fulfill the load demands. DC bus voltage regulation under constant load demand can be observed from Fig. 30. C-HIL experimental result shows spikes of few volts which is in the acceptable range illustrating a satisfactory performance of the controllers.

Figs. 31 and 32 display battery and SC currents respectively under variable load demands. DC bus voltage regulation under variable load demands has been shown in Fig. 33. It can be observed that the experimental and simulation results of battery and SC currents exhibit an acceptable behavior. DC bus voltage has been maintained to its nominal voltage despite load changes which shows the efficient working of the proposed framework.

7. Conclusion

In this research article, renewable energy sources consisting of wind and PV along with energy storage system consisting of a battery and a supercapacitor integrated with DC bus have been presented. For the control of the power sources, supertwisting sliding mode controllers have been implemented to operate

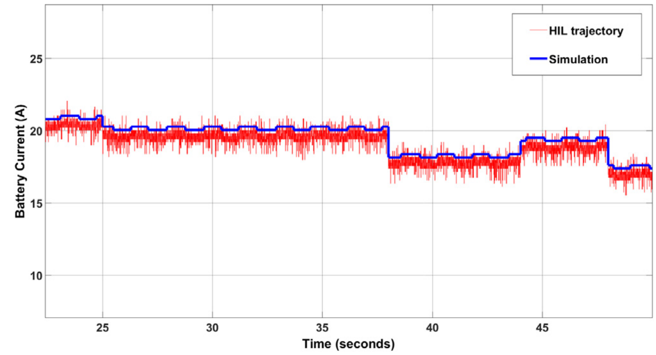

Fig. 28. Battery current I_b in case of constant load.

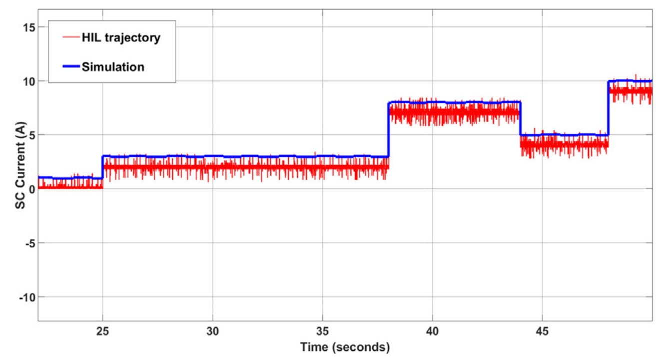

Fig. 29. SC current I_{sc} in case of constant load.

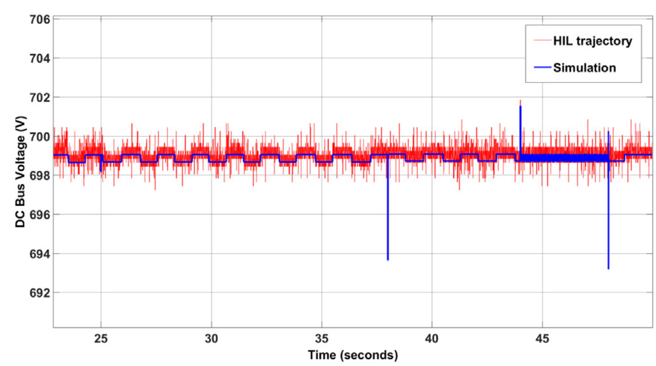

Fig. 30. DC bus voltage V_{DC} in case of constant load.

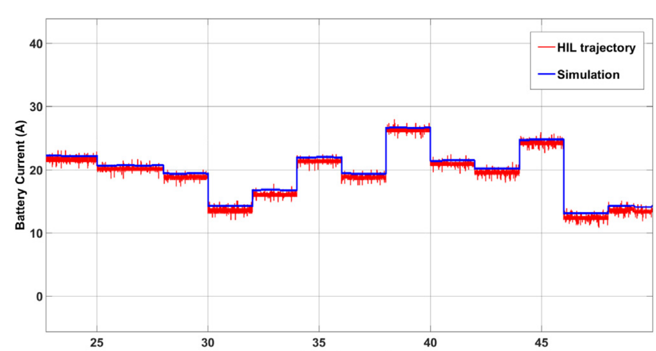

Fig. 31. Battery current I_b in case of varying load.

them at their maximum power points and to maintain power balance between RESs and ESS. The proposed control strategy

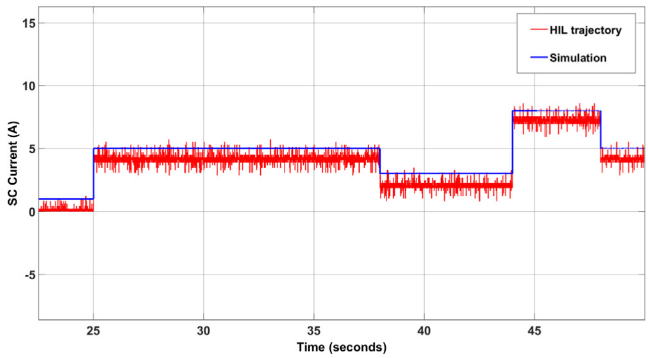

Fig. 32. SC current I_{sc} in case of varying load.

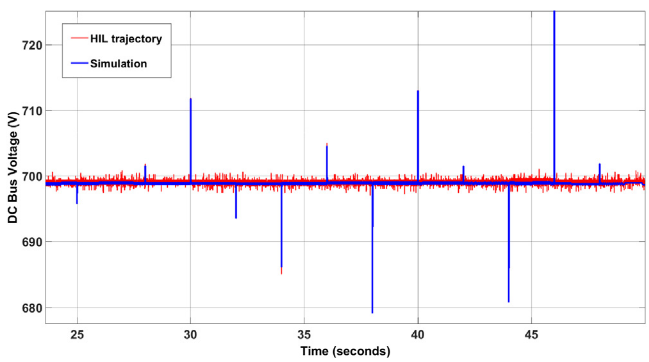

Fig. 33. DC bus voltage V_{DC} in case of varying load.

allows power management between RESs and ESS to fulfill the load requirements. The system's global asymptotic stability has been verified using the Lyapunov analysis. The proposed controllers along with an energy management system based on fuzzy logic have been simulated in MATLAB/Simulink® (2019a) to verify the performance of the designed framework. A comparison with sliding mode and integral sliding mode controllers has been performed which reveals that the performance of the proposed STSMC surpass them in terms of the DC bus voltage regulation as well as the transient responses of the states. Controller hardware-in-the loop experiments validate the performance of the proposed controllers which ensures that the ESS supports RESs during high load demands which helps in increasing the life-span of RESs. In the future, this work can be extended to the grid-connected mode and additional sources can be integrated with the grid i.e. proton exchange membrane fuel cell to lessen the dependency on ESS. The power flow between the RESs and ESS in a DC microgrid and the main grid can be maintained by designing an EMS using various control algorithms.

Declaration of competing interest

The authors declare that they have no known competing financial interests or personal relationships that could have appeared to influence the work reported in this paper.

Appendix

Tables 3–6 present the specifications of the simulated system.

Table 3
Parameters of wind energy system.

Wind Turbine Model	
Air density	1.225 kg/m^3
Rotor diameter	5.5 m
C_{p-max}	0.45
λ_{opt}	8.1
Rated wind speed	5 m/s
PMSG Parameters	
Stator phase resistance	0.425 Ω
Armature inductance	0.000395 H
Flux linkage	0.433
Inertia	0.01197 kg/m^2
Viscous damping	0.001189 Nms

Table 4
Parameters of PV energy system.

PV array model	
PV module per string	10
Parallel connected strings	1
Number of cells per module	60
Open circuit voltage	363 V
Short circuit current	7.84 A
Voltage at MPP	290 V
Current at MPP	7.35 A
Maximum power per module	2.1 kW

Table 5
Parameters of energy storage system.

Lead Acid Battery	
Voltage	540 V
Rated capacity	33.9 Ah
Maximum charge current	17.5 A
Maximum discharge current	30 A
Supercapacitor Bank	
Voltage	205 V
Rated capacity	2700 F

Table 6
Parameters of the simulated DC microgrid.

DC-DC converters parameters	
L_w, L_{pv}, L_b, L_{sc}	20 mH, 20 mH, 3.3 mH, 3.3 mH
R_w, R_b, R_{sc}	20 mΩ, 20 mΩ, 20 mΩ
C_w, C_{pv}, C_{pout}, C_{DC}	68 μF, 68 μF, 68 μF, 68 μF
Switching frequency	100 kHz
Gains used in simulated control system	
a_1, a_3, a_6, a_7	0.1, 0.1, 0.5, 0.06
k_1, k_2, k_3, k_4, k_6, k_7, k_8, k_9	1000, 1000, 1000, 3000, 9500, 10000, 2000, 1000
α, β, ζ, γ	0.5, 0.2, 0.5, 0.5
ϕ_1, ϕ_3, ϕ_6, ϕ_7	0.5, 0.5, 0.5, 0.5

References

[1] Khare V, Nema S, Baredar P. Solar–wind hybrid renewable energy system: A review. Renew Sustain Energy Rev 2016;58:23–33, [Online]. Available: http://dx.doi.org/10.1016/j.rser.2015.12.223.

[2] Zeng B, Zhang J, Yang X, Wang J, Dong J, Zhang Y. Integrated planning for transition to low-carbon distribution system with renewable energy generation and demand response. IEEE Trans Power Syst 2013;29(3):1153–65, [Online]. Available: http://dx.doi.org/10.1109/TPWRS.2013.2291553.

[3] Rahbar K, Chai CC, Zhang R. Energy cooperation optimization in microgrids with renewable energy integration. IEEE Trans Smart Grid 2016;9(2):1482–93, [Online]. Available: http://dx.doi.org/10.1109/TSG.2016.2600863.

[4] Loh PC, Li D, Chai YK, Blaabjerg F. Hybrid AC-DC microgrids with energy storages and progressive energy flow tuning. IEEE Trans Power Electron 2012;28(4):1533–43, [Online]. Available: http://dx.doi.org/10.1109/TPEL.2012.2210445.

[5] Guerrero JM, Chandorkar M, Lee T-L, Loh PC. Advanced control architectures for intelligent microgrids—Part I: Decentralized and hierarchical

control. IEEE Trans Ind Electron 2012;60(4):1254–62, [Online]. Available: http://dx.doi.org/10.1109/TIE.2012.2194969.

[6] Khorsandi A, Ashourloo M, Mokhtari H, Iravani R. Automatic droop control for a low voltage DC microgrid. IET Gener Transm Distrib 2016;10(1):41–7, [Online]. Available: http://dx.doi.org/10.1049/iet-gtd.2014.1228.

[7] Lu M-S, Chang C-L, Lee W-J, Wang L. Combining the wind power generation system with energy storage equipment. IEEE Trans Ind Appl 2009;45(6):2109–15, [Online]. Available: http://dx.doi.org/10.1109/TIA.2009.2031937.

[8] Liu Y, Du W, Xiao L, Wang H, Bu S, Cao J. Sizing a hybrid energy storage system for maintaining power balance of an isolated system with high penetration of wind generation. IEEE Trans Power Syst 2015;31(4):3267–75, [Online]. Available: http://dx.doi.org/10.1109/TPWRS.2015.2482983.

[9] Iftikhar R, Ahmad I, Arsalan M, Naz N, Ali N, Armghan H. MPPT for photovoltaic system using nonlinear controller. Int J Photoenergy 2018;2018. [Online]. Available: http://dx.doi.org/10.1155/2018/6979723.

[10] Xu L, Cheng R, Yang J. A new MPPT technique for fast and efficient tracking under fast varying solar irradiation and load resistance. Int J Photoenergy 2020;2020. [Online]. Available: http://dx.doi.org/10.1155/2020/6535372.

[11] Kumar PS, Chandrasena R, Ramu V, Srinivas G, Babu KVSM. Energy management system for small scale hybrid wind solar battery based microgrid. IEEE Access 2020;8:8336–45, [Online]. Available: http://dx.doi.org/10.1109/ACCESS.2020.2964052.

[12] Datta U, Kalam A, Shi J. Hybrid PV-wind renewable energy sources for microgrid application: an overview. In: Hybrid-renewable energy systems in microgrids. Elsevier; 2018, p. 1–22, [Online]. Available: http://dx.doi.org/10.1016/B978-0-08-102493-5.00001-7.

[13] Bambang RT, Rohman AS, Dronkers CJ, Ortega R, Sasongko A, et al. Energy management of fuel cell/battery/supercapacitor hybrid power sources using model predictive control. IEEE Trans Ind Inf 2014;10(4):1992–2002, [Online]. Available: http://dx.doi.org/10.1109/TII.2014.2333873.

[14] Rahman AU, Ahmad I, Malik AS. Variable structure-based control of fuel cell-supercapacitor-battery based hybrid electric vehicle. J Energy Storage 2020;29:101365, [Online]. Available: http://dx.doi.org/10.1016/j.est.2020.101365.

[15] Arsalan M, Iftikhar R, Ahmad I, Hasan A, Sabahat K, Javeria A. MPPT for photovoltaic system using nonlinear backstepping controller with integral action. Sol Energy 2018;170:192–200, [Online]. Available: http://dx.doi.org/10.1016/j.solener.2018.04.061.

[16] El Khateb A, Rahim NA, Selvaraj J, Uddin MN. Fuzzy-logic-controller-based SEPIC converter for maximum power point tracking. IEEE Trans Ind Appl 2014;50(4):2349–58, [Online]. Available: http://dx.doi.org/10.1109/TIA.2014.2298558.

[17] Justo JJ, Mwasilu F, Lee J, Jung J-W. AC-microgrids versus DC-microgrids with distributed energy resources: A review. Renew Sustain Energy Rev 2013;24:387–405, [Online]. Available: http://dx.doi.org/10.1016/j.rser.2013.03.067.

[18] Opiyo NN. A comparison of DC-versus AC-based minigrids for cost-effective electrification of rural developing communities. Energy Rep 2019;5:398–408, [Online]. Available: http://dx.doi.org/10.1016/j.egyr.2019.04.001.

[19] Lonkar M, Ponnaluri S. An overview of DC microgrid operation and control. In: The sixth international renewable energy congress. IEEE; 2015, p. 1–6, [Online]. Available: http://dx.doi.org/10.1109/IREC.2015.7110892.

[20] Li X, Guo L, Zhang S, Wang C, Li YW, Chen A, et al. Observer-based DC voltage droop and current feed-forward control of a DC microgrid. IEEE Trans Smart Grid 2017;9(5):5207–16, [Online]. Available: http://dx.doi.org/10.1109/TSG.2017.2684178.

[21] Liu J, Zhang W, Rizzoni G. Robust stability analysis of DC microgrids with constant power loads. IEEE Trans Power Syst 2017;33(1):851–60, [Online]. Available: http://dx.doi.org/10.1109/TPWRS.2017.2697765.

[22] Etemadi AH, Davison EJ, Iravani R. A generalized decentralized robust control of islanded microgrids. IEEE Trans Power Syst 2014;29(6):3102–13, [Online]. Available: http://dx.doi.org/10.1109/TPWRS.2014.2312615.

[23] Kumar M, Srivastava S, Singh S. Control strategies of a DC microgrid for grid connected and islanded operations. IEEE Trans Smart Grid 2015;6(4):1588–601, [Online]. Available: http://dx.doi.org/10.1109/TSG.2015.2394490.

[24] Babazadeh M, Karimi H. A robust two-degree-of-freedom control strategy for an islanded microgrid. IEEE Trans Power Delivery 2013;28(3):1339–47, [Online]. Available: http://dx.doi.org/10.1109/TPWRD.2013.2254138.

[25] Du Z, Kao Y, Karimi HR, Zhao X. Interval type-2 fuzzy sampled-data H_∞ control for nonlinear unreliable networked control systems. IEEE Trans Fuzzy Syst 2019. [Online]. Available: https://doi.org/10.1109/TFUZZ.2019.2911490.

[26] Du Z, Kao Y, Zhao X. An input delay approach to interval type-2 fuzzy exponential stabilization for nonlinear unreliable networked sampled-data control systems. IEEE Trans Syst Man Cybern: Syst 2019. [Online]. Available: https://doi.org/10.1109/TSMC.2019.2930473.

[27] Du Z, Kao Y, Park JH. New results for sampled-data control of interval type-2 fuzzy nonlinear systems. J Franklin Inst B 2020;357(1):121–41, [Online]. Available: https://doi.org/10.1016/j.jfranklin.2019.09.035.

[28] Iovine A, Siad SB, Damm G, De Santis E, Di Benedetto MD. Nonlinear control of a DC microgrid for the integration of photovoltaic panels. IEEE Trans Autom Sci Eng 2017;14(2):524–35, [Online]. Available: http://dx.doi.org/10.1109/TASE.2017.2662742.

[29] Hassan MA, Li E-p, Li X, Li T, Duan C, Chi S. Adaptive passivity-based control of dc–dc buck power converter with constant power load in dc microgrid systems. IEEE J Emerg Sel Top Power Electron 2018;7(3):2029–40, [Online]. Available: http://dx.doi.org/10.1109/JESTPE.2018.2874449.

[30] Roy TK, Mahmud MA, Oo AM. Operations of DC microgrids in coordination with AC grids based on nonlinear backstepping controllers. In: 2018 IEEE power & energy society general meeting. IEEE; 2018, p. 1–5, [Online]. Available: http://dx.doi.org/10.1109/PESGM.2018.8585994.

[31] Roy TK, Mahmud MA, Oo AMT, Haque ME, Muttaqi KM, Mendis N. Nonlinear adaptive backstepping controller design for islanded DC microgrids. IEEE Trans Ind Appl 2018;54(3):2857–73, [Online]. Available: http://dx.doi.org/10.1109/TIA.2018.2800680.

[32] Baghaee HR, Mirsalim M, Gharehpetian GB, Talebi HA. A decentralized power management and sliding mode control strategy for hybrid AC/DC microgrids including renewable energy resources. IEEE Trans Ind Inf 2017. [Online]. Available: http://dx.doi.org/10.1109/TII.2017.2677943.

[33] Ghiasi MI, Golkar MA, Hajizadeh A. Lyapunov based-distributed fuzzy-sliding mode control for building integrated-DC microgrid with plug-in electric vehicle. IEEE Access 2017;5:7746–52, [Online]. Available: http://dx.doi.org/10.1109/ACCESS.2017.2689807.

[34] Tse CK, Di Bernardo M. Complex behavior in switching power converters. Proc IEEE 2002;90(5):768–81, [Online]. Available: https://doi.org/10.1109/JPROC.2002.1015006.

[35] Sanders SR. Nonlinear control of switching power converters [Ph.D. dissertation], Massachusetts Institute of Technology; 1989.

[36] Nasiri M, Milimonfared J, Fathi S. Modeling, analysis and comparison of TSR and OTC methods for MPPT and power smoothing in permanent magnet synchronous generator-based wind turbines. Energy Convers Manage 2014;86:892–900, [Online]. Available: http://dx.doi.org/10.1016/j.enconman.2014.06.055.

[37] Rivera J, Garcia L, Mora C, Raygoza JJ, Ortega S. Super-twisting sliding mode in motion control systems. In: Sliding mode control. Croatia: InTech Rijeka; 2011, p. 237–54.

[38] Moreno JA, Osorio M. A Lyapunov approach to second-order sliding mode controllers and observers. In: 2008 47th IEEE conference on decision and control. IEEE; 2008, p. 2856–61, [Online]. Available: https://doi.org/10.1109/CDC.2008.4739356.

[39] Messalti S, Harrag AG, Loukriz AE. A new neural networks MPPT controller for PV systems. In: The sixth international renewable energy congress. IEEE; 2015, p. 1–6, [Online]. Available: http://dx.doi.org/10.1109/IREC.2015.7110907.

[40] Zadeh LA. Fuzzy sets. Inf Control 1965;8(3):338–53, [Online]. Available: http://dx.doi.org/10.1016/S0019-9958(65)90241-X.

[41] Armghan H, Yang M, Wang M, Ali N, Armghan A. Nonlinear integral backstepping based control of a DC microgrid with renewable generation and energy storage systems. Int J Electr Power Energy Syst 2020;117:105613, [Online]. Available: http://dx.doi.org/10.1016/j.ijepes.2019.105613.